Total electron and proton energy input during auroral substorms: Remote sensing with IMAGE-FUV

B. Hubert,[1] J.-C. Gérard,[1] D. S. Evans,[2] M. Meurant,[1]
S. B. Mende,[3] H. U. Frey,[3] and T. J. Immel[3]

Received 21 December 2001; revised 15 February 2002; accepted 4 March 2002; published 14 August 2002.

[1] The IMAGE satellite carries three FUV imagers observing N_2 LBH, O I 1356 Å, and HI Lyman α emissions in the polar aurora. These simultaneous observations are used to characterize the precipitating electron and proton energy fluxes. The proton energy flux is derived from the Lyman α measurements on the basis of efficiency curves calculated with a Monte Carlo simulation of the proton aurora. The resulting proton contribution to the N_2 LBH and O I 1356 Å emissions is calculated and subtracted to obtain the electron contribution in the other two channels. These two quantities are used to determine the precipitating electron average energy and energy flux. The proton and electron energy fluxes are integrated over the hemisphere to obtain the rate of auroral energy dissipation (hemispheric power) carried by the protons and electrons separately. The time development of the proton and electron aurora during four winter time events is examined. Although the onsets of the proton and electron aurora coincide in time and space, the time of the peak of energy dissipation and the recovery time are often found to differ. The fractional energy flux carried by the protons is highest during quiet periods and reaches a minimum during the most active phase of the substorms. This result is in agreement with the dependence of the fractional proton hemispheric power on magnetic activity measured by NOAA 15. The hemispheric power deduced from the FUV images is compared to the NOAA-deduced values and found to be in reasonable agreement. Sources of uncertainties in the determination of the hemispheric power are discussed on the basis of several sensitivity tests. In particular, it is found that the most critical factor is the assumption made on the energy of the auroral protons if this energy is <25 keV. *INDEX TERMS:* 0358 Atmospheric Composition and Structure: Thermosphere—energy deposition; 0310 Atmospheric Composition and Structure: Airglow and aurora; 2716 Magnetospheric Physics: Energetic particles, precipitating; 2788 Magnetospheric Physics: Storms and substorms; *KEYWORDS:* Substorm, proton, electron, energy, IMAGE-FUV

1. Introduction

[2] The concept of the auroral substorm was first introduced by *Akasofu* [1964] on the basis of sequences of ground based auroral images obtained with all-sky cameras. The availability of auroral images [*Craven and Frank*, 1985] with the Dynamics Explorer 1 auroral imager made it possible to follow the onset and development of auroral substorms from a global vantage point. Auroral precipitation produces ionization which considerably enhances the ionospheric Pedersen conductivity and produces Joule heating in the presence of an electric field. In addition, part of the energy of the auroral particles is dissipated into local heating through dissociation and exothermic chemical reactions [*Singh and Gérard*, 1982]. As a consequence of the time variation of the auroral energy injected into the polar thermosphere, the amount of particle and Joule heating significantly varies with time and in space. Based on a statistical analysis of measurements carried by the Defense Meteorological Satellite Program (DMSP), *Hardy et al.* [1989] found that the auroral energy flux is mostly carried by electrons which contribute 85% to 90% of the total input. Ions, mainly protons, carry the rest of the energy.

[3] The total hemisphere power (HP) is a measure of the instantaneous rate of auroral energy injection into the atmosphere of one hemisphere. It has been deduced from ground-based measurements and correlated with auroral activity indices such as AE, AU and AL [*Ahn et al.*, 1983; *Richmond et al.*, 1990; *Lu et al.*, 1998]. With the availability of ultraviolet images, HPs can be obtained by integrating the auroral brightness observed in selected spectral band provided that the relationship between the instrumental count rate and the absolute incident flux of auroral particles is well known.

[4] *Lummerzheim et al.* [1997] derived the time evolution of the HP during a 10-hour period from observations carried

Laboratoire de Physique Atmosphérique et Planétaire, Université de Liège, Liège-Ougrée, Belgium
NOAA Space Environment Center, Boulder, Colorado, USA
Space Sciences Laboratory, University of California, Berkeley, California, USA

0148-0227/02/2001JA009229$09.00

with the Ultraviolet Imager (UVI) on board the POLAR spacecraft. The values ranged from nearly 0 to 125 GW and compared reasonably well with the NOAA-derived HPs. The 5-minute resolution of the UVI data was shown to provide a substantial improvement in the time resolution of HPs. However, the POLAR UVI instrument is not able to discriminate between proton and electron-induced LBH emissions. The derived HP can thus only be calculated assuming that excitation is solely due to auroral electron impact on N_2. *Østgaard et al.* [2002] combined observations of the UVI and the X-ray Imaging Experiment (PIXIE) to derive the total energy dissipation for 4 days in 1997, with a 5-minute resolution. They found that during substorms, the energy dissipation is linearly related to the square root of the AE and AL indices.

[5] On the basis of a statistical study of DMSP satellite particle measurements, *Hardy et al.* [1989] observed a fractional contribution of protons to the total hemispheric power of 14.5% for Kp = 1, dropping to 10% for Kp = 3. This study needed extrapolation of the proton spectra for energies above 30 keV. *Hardy et al.* [1989] used a maxwellian distribution for this extrapolation, leading to a possible underestimate of the proton flux and fraction. Nevertheless, this suggests an activity dependence of the proton fraction which will be investigated in this work.

[6] The Total Energy Detectors (TED) on board the NOAA-TIROS satellites provide estimates of the HP for both hemispheres. The satellites are on a circular quasi-polar orbit near 850 km. The TEDs integrate the precipitated energy flux measured separately for electrons and protons from 50 eV to 20 keV. The estimate is based on a comparison between the latitude weighted integration of the energy flux measured along the satellite track of a NOAA-TIROS spacecraft and climatology maps of the energy flux obtained from the NOAA database. The maps are based on 10 levels of hemispheric power roughly corresponding to Kp indices from 0 to 5+. The magnitude of the precipitating energy flux measured along the NOAA orbit is matched to one of the 10 to estimate the total hemispheric power [*Fuller-Rowell and Evans*, 1987]. This methodology assumes that the auroral particle energy influxes follow the characteristic patterns given by the climatology maps. This assumption is not valid during dynamic times (substorms, for example) when there are strong magnetic local time gradients in the energy influx and estimates of hemispheric power during such times may not be accurate. In spite of these limitations, the NOAA HP is frequently used in studies of the solar-terrestrial events and can be used as an input parameter to the TIGCM NCAR model by *Roble et al.* [1988].

[7] A further breakthrough has recently been achieved with the FUV experiment onboard the Imager for Magnetopause-to-Aurora Global Exploration) (IMAGE) satellite [*Burch et al.*, 2001] that provides simultaneous images of the electron and proton aurora. The IMAGE-FUV images thus allow to distinguish the proton and electron auroral activities at a global scale.

[8] In this study, we separately derive the hemispheric power associated with auroral protons and electrons, using the data from the Spectrographic Imager (SI12 and SI13) and the Wideband Imaging Camera (WIC) instruments onboard the IMAGE satellite. Section 2 presents the IMAGE-FUV imagers and the method used to calculate the proton and electron hemispheric powers. Section 3 describes four substorm case studies and results concerning the relative importance of the proton precipitation. To assess the importance of sources of uncertainties, a substorm observed on December 25, 2000 has been processed under different assumptions. Section 4 describes the sensitivity of the deduced hemispheric power to the atmospheric composition, the assumed proton average energy and the viewing geometry. The last section discusses some of the findings concerning the relative importance of protons and presents NOAA-TIROS measurements confirming the decrease of the fraction of energy carried by protons during active periods.

2. Calculation of the Hemispheric Power

[9] We first briefly review the set of FUV instruments and the model used to calculate the dependence of the emission efficiency on the energy of the auroral particles. We then describe the methodology used to derive the time series of hemispheric powers.

2.1. IMAGE-FUV Imagers

[10] The IMAGE satellite is in an eccentric orbit with a 1000-km perigee and $\sim$7 Earth radii apogee. The FUV experiment consists of three imagers working simultaneously at different wavelengths [*Mende et al.*, 2000a, 2000b]. The Wideband Imaging Camera (WIC) remotely senses the atmospheric and auroral emission in the 1400–1800 Å domain, where the bulk of the N_2 LBH bands is emitted. The Spectrographic Imager (SI) has two channels operating at 1356 Å (SI13) and 1218 Å (SI12) respectively. The Spectrographic Imager at 1356 Å (SI13) obtains images in the 1300–1400 Å wavelength interval (FWHM = 50 Å). As the atmospheric O_2 absorption varies in these wavelength intervals, the ratio of the WIC and SI13 measurements is sensitive to the depth at which the precipitating particles cause some excitation, and is thus sensitive to the average energy of the particles. Consequently the simultaneous measurements of these two instruments can be used to estimate the electron average energy and energy flux. The SI13 passband is shown in Figure 1, together with the WIC passband and the laboratory spectrum of the N_2 LBH emission by *Ajello and Shemansky* [1985]. As auroral electrons collide with the main constituents, N_2 molecules can be excited or dissociated into two nitrogen atoms, usually excited as well. These excited nitrogen atoms will also emit photons, some of them falling inside the WIC or SI13 bandpass.

[11] The SI12 instrument provides global imaging of the proton aurora for the first time. Its response function was described in detail by *Mende et al.* [2000b]. *Gérard et al.* [2001] showed that the SI12 observations are in good quantitative agreement with the values predicted from DMSP and FAST in-situ proton measurements. The instrument efficiently rejects the geocoronal Ly α emission and only Doppler shifted Ly α photons are detected. These photons are solely due to precipitating protons that capture an electron in an inelastic collision with the ambient gas particles [*Vallance-Jones*, 1974; *Rees*, 1989]. The hydrogen atom formed in this process can be excited in the H(2s) state

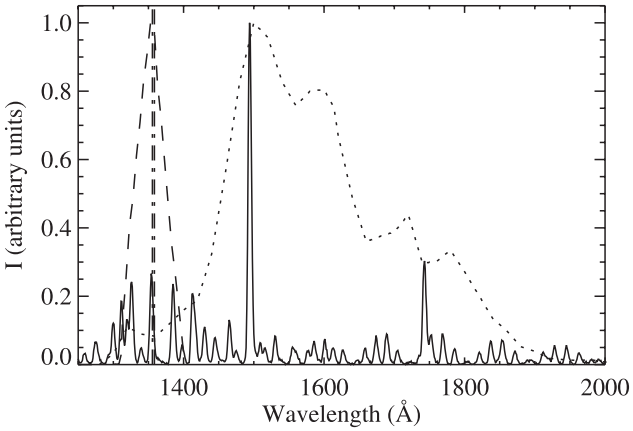

Figure 1. Response functions of the WIC (dotted line) and SI13 imagers (dashed line) and laboratory N_2 LBH spectrum [*Ajello and Shemansky*, 1985] (solid line). The position of the 1356 A doublet is also indicated (dash-dot line).

and relax by emitting a Ly α photon which is Doppler shifted according to the relative velocity between the emitting particle and the spacecraft.

[12] The three instruments simultaneously obtain images of the planet once every two minutes as the IMAGE satellite spins [*Frey et al.*, 2001]. The correction for satellite spin is made using the Time Delay Integration (TDI) technique. This instrumental setup gives an unprecedented time resolution. The signal integration time is ~10 seconds for the WIC camera, and ~5 seconds for both SI's. With these exposure times, the sensitivities at the transmission peaks of the instruments are 714 AD units/kR (Analog Digital Unit) for WIC, 14.9 counts/kR for SI13 and 24.8 counts/kR for SI12 [*Gladstone et al.*, 2000].

[13] The WIC camera has a ~17° field of view and produces 256 × 256 pixel images, giving a ~52 km resolution from apogee. The instrument point spread function (PSF) FWHM is estimated at ~3.5 pixels. The SI13 and SI12 cameras generate 128 × 128 pixel images with a ~16° and 17° FOV respectively, so that, from distance of ~7 Earth radii, a pixel projects to a square of ~97 × 97 (~103 × 103) km^2 respectively. The PSF FWHM's are ~2 pixels for SI12 and ~1.5 pixel for SI13.

[14] Several works did compare the IMAGE-FUV data with simultaneous in-situ particle flux measurements. As already pointed out, *Gérard et al.* [2001] compared the FAST and DMSP ion flux measurements with the SI12 images. The IMAGE-FUV data were also compared with the ion and electron measurements of the FAST [*Frey et al.*, 2001] and NOAA [*Coumans et al.*, 2002] satellites. All these studies gave a satisfactory agreement between the IMAGE-FUV observations and the in-situ particles measurements. We now describe how the IMAGE-FUV data are combined to study the aurora and its energy characteristics.

2.2. Auroral Precipitation Derived From IMAGE-FUV

2.2.1. Electron aurora

[15] The Wideband Imaging Camera (WIC) and the Spectrographic Imager at 1356 Å (SI13) are used to determine the mean energy and the total flux of the precipitating electrons. Since two different quantities are measured, two other quantities can be deduced, based on assumptions for the other parameters. Theoretical efficiency curves as a function of average electron energy and view angle have thus been calculated for the O I 1356 Å and LBH emissions as well as the associated WIC and SI13 count rates. We use the GLOW model [*Solomon et al.*, 1988] updated and extended in energy range [*Solomon*, 2001] for a unit incident Maxwellian electron flux [*Hubert et al.*, 2001]. The integration along the line of sight was calculated assuming the spatial distribution of the volume emission rate were spherically symmetric. This assumption avoids the necessity for a full 3-D treatment, which would require prohibitively high computational cost. The assumption is valid as long as the tangent height is below ~5600 km (geocentric altitude, i.e. counted from Earth center), that is for angles with the local zenith at an altitude of 120 km (counted from Earth surface) less than ~60°. A typical MSIS [*Hedin*, 1991] atmosphere profile was adopted. The MSIS parameters are for December 24, 1630 UT, a latitude of 65°, a longitude of 0°, solar maximum conditions with F10.7A = 216, F10.7 = 205, and a geomagnetic index Ap of 6.

[16] As the two instruments operate at different wavelengths, the effect of O_2 absorption is different for the two imagers, and thus the WIC and SI13 signals are dependent upon the average electron energy which controls the altitude profile of photon emission. The average electron energy may thus be estimated from the ratio of the WIC to SI13 measurements. Figure 2a shows the WIC and SI13 efficiency curves as a function of the electron energy for a vertical viewing. Figure 2b shows the ratio of these curves

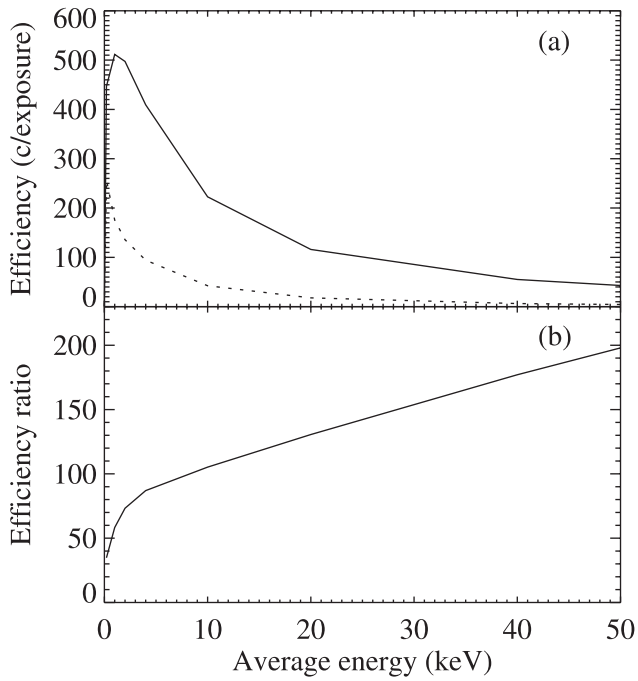

Figure 2. Panel a shows the WIC efficiency (solid line) and the SI13 efficiency multiplied by 20 (dotted line), expressed in counts/pixel per exposure versus the electron average energy. The ratio of the WIC to SI13 efficiencies is shown in panel b. The initial electron energy distribution is assumed to be Maxwellian.

which monotonically increases with the electron energy, reflecting both the change of the differential optical thickness and the variation of the atmospheric composition with altitude.

[17] The general procedure for combining the WIC and SI13 simultaneous observations of the same location may be summarized in the following simple operations:

(1) map the SI13 128×128 pixel image into a WIC 256 × 256 pixel space;

(2) compute the WIC/SI13 ratio from the observations and deduce the electron average energy for each pixel using the curve in Figure 2b;

(3) use the most sensitive instrument (i.e. WIC) measurement and its efficiency value at the calculated average energy to determine the energy flux for each pixel. The efficiency curves appropriate to the actual viewing angle are used.

2.2.2. Proton aurora

[18] The viewing geometry influences the proton auroral observations in two different ways. A slant line of sight has a longer path into the atmosphere than a vertical line of sight leading to an increased brightness associated with non-vertical observations. Additionally, the Doppler-shifted wavelength of the Ly α photons depends of the angle between the line of sight and the velocity vector of the emitting particle. Therefore, for a given precipitating proton flux, the line shape and wavelength of the line peak depend on the viewing angle and thus the fraction of the emitted photons getting inside the passband is a function of the viewing geometry. The proton average energy will also modify the line shape and the emission rate vertical profile, both in its peak altitude and column emission rate, owing to the cross sections energy dependence of the proton (and hydrogen) collision processes with the atmospheric constituents. Observation of the proton aurora with SI12 is thus more complex [*Gérard et al.*, 2001]. A Monte Carlo model [*Gérard et al.*, 2000] was used to derive efficiency curves giving the line brightness and SI12 count rate as a function of the view angle and proton average energy. We assume that the protons have a kappa distribution with a κ index of 3.5 [*Hubert et al.*, 2001]. The line of sight integration is computed assuming the spatial distribution of the auroral emission is spherically symmetric. The analysis of each SI12 image is based on these efficiencies and thus requires an assumption of the proton's characteristic energy. We use *Hardy et al.* [1991] empirical model that gives the average energy and the energy flux of the protons as a function of the Kp index and the magnetic latitude and local time.

[19] Proton precipitation not only produces hydrogen emission, but also a direct excitation of atmospheric components and ionization of the ambient thermospheric gas. The produced electrons will impinge upon the neutral gas particles, generating additional excitation and ionization, similar to an electron aurora. The direct excitation of the LBH and NI lines and O I 1356 Å, and the ionization rate, (i.e. the secondary electron production rate) of the proton aurora are calculated by the Monte Carlo model as well. The ionization rate is used as an input in the electron aurora model. Efficiency curves depending on the proton average energy are thus obtained for the LBH and O I 1356 Å emissions as well as the associated WIC and SI13 count rates (with viewing geometry dependence) associated with the proton aurora. This procedure allows for a subtraction of the proton induced signal in the WIC and SI13 count rates, so that the electron contribution can be calculated: the proton average energy comes from the empirical model of *Hardy et al.* [1991] (see preceding paragraph), and the proton energy flux is determined using the SI12 image and efficiency. The calculated WIC and SI13 efficiency curves specific of the proton precipitation (including its secondary electrons) are then used to obtain the contribution to be subtracted from the WIC and SI13 images in order to isolate the electron contribution. This procedure is applied to each pixel of the images.

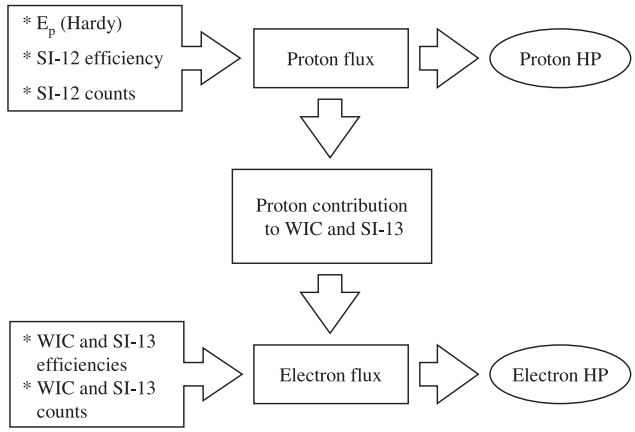

Figure 3. Methodology used to derive the hemispheric power for electron and proton from a set of WIC, SI12 and SI13 images (see text).

2.3. Auroral Hemispheric Power

[20] The method described before has been applied to the entire auroral region of each image used in this study. We selected winter time observations to minimize the dayglow contribution in the auroral zone. After the local energy flux is determined (for both protons and electrons) in each pixel, the HP is obtained by multiplying this flux by the area of each pixel and summing over all regions of auroral emission. The area of each pixel is calculated from the pointing information of the spacecraft. The procedure is summarized in Figure 3 and is applied to each set of three images obtained every 2 minutes. Some of these steps depend on factors such as the determination of the proton mean energy, the approximation on horizontal homogeneity and the neutral thermospheric composition. The influence of these factors upon the final results will be discussed in section 4.

3. Substorm Case Studies

[21] We present four selected substorms which occurred on November 27, December 9 and 25, 2000 and January 30, 2001, observed in the north hemisphere. We will also briefly describe the solar wind context of the events as measured by the Advanced Composition Explorer (ACE) satellite. We first focus on the December 25 event, a set of two substorms following a very quiet period.

3.1. December 25, 2000

[22] On December 25, around 1145 UT, the ACE satellite located at the L1 Lagrange point $\sim 1.51 \times 10^6$ km from the

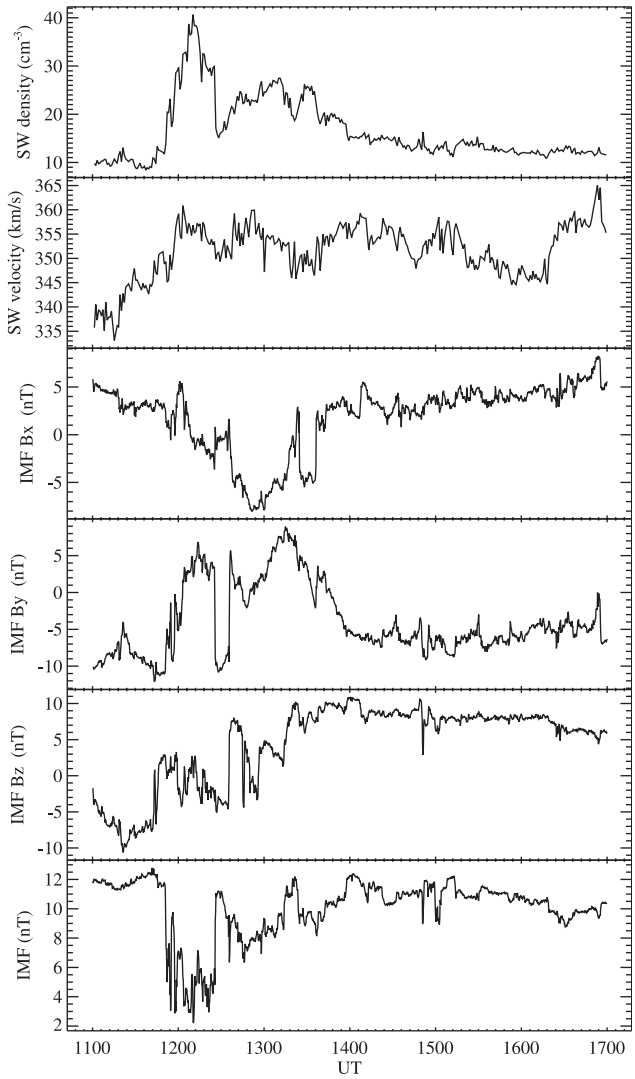

Figure 4. Solar wind characteristics measured by the ACE satellite on December 25, 2000 during the period of FUV observations.

Earth, measured a sudden increase in the solar wind density from ~10 cm^{-3} at 1145 to a maximum value of ~40 cm^{-3} at 1210 UT (Figure 4).

[23] The solar wind bulk velocity was ~360 km s^{-1} at 1200 UT. As shown in Figure 4, the interplanetary magnetic field magnitude (IMF) remained rather stable at ~12 nT until ~1150 when it abruptly dropped, reaching a value of ~5 nT at ~1150. The Bz component displayed a rapid pulse from −8 nT to +0.5 nT, before dropping to −7 nT between 1140 and 1145, when it turned positive at 1150. Bz remained positive or nearly zero until ~1200 UT when it turned negative again. The By component encountered large variations between −10 and −1 nT, but remained negative until ~1205 UT, when it changed sign. The time variation of Bx and By are also shown in Figure 4. At a velocity of 355 km s^{-1} typical for this event, the distance between the ACE satellite and the Earth is traveled in ~70 minutes. An auroral response to the solar wind variations is therefore expected at approximately 1300 UT. Figure 5 shows three images measured by the WIC, SI13 and SI12 instruments at 1256, 1302 and 1324 UT with the onset clearly appearing in all three imagers at 1302 UT.

[24] Figure 6 presents the hemispheric power calculated using the IMAGE-FUV measurements between 1300 and 1600 UT following the procedure described in section 2.3. The WIC and SI13 images show a visually determined substorm onset at 1300 in the premidnight sector of the oval, consistent with the ACE satellite measurements. This disturbance followed a very quiet 12-hour period with Ap < 4 and AE and AL below 20 nT for more than 24 hours. During the substorm, the Kp index reached 3, with AE and AL up to ~500 nT at 1320 UT. Dst was quiet with its largest value of −13 nT between 1500 and

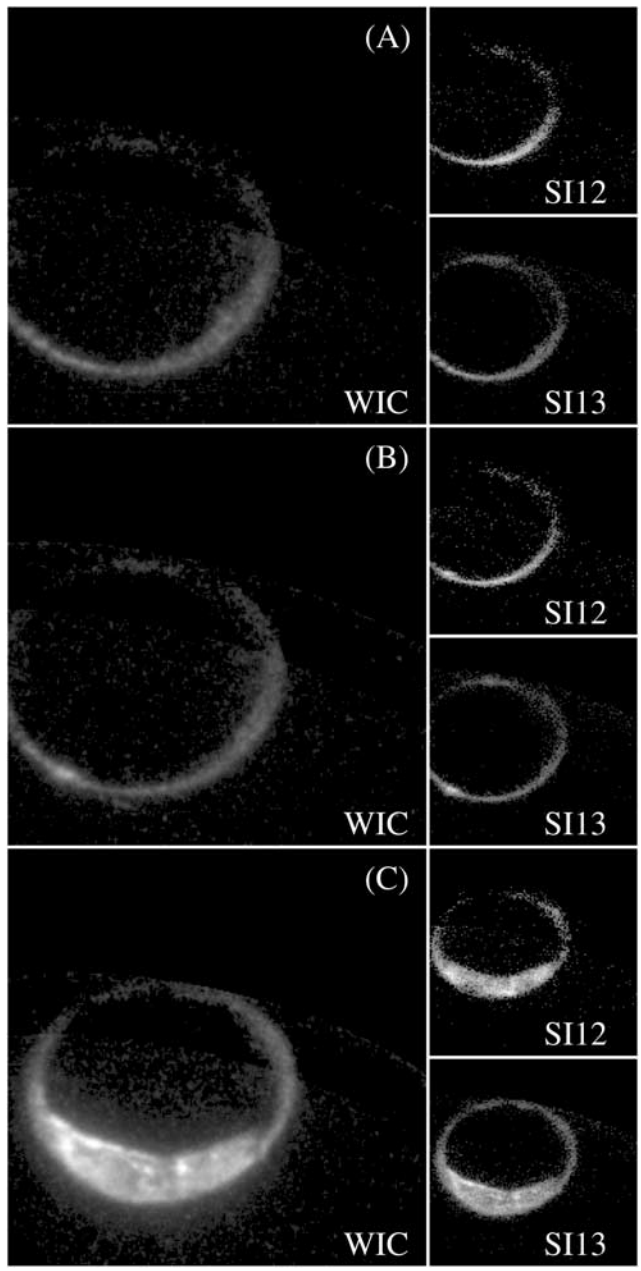

Figure 5. Three consecutive sets of WIC, SI13 and SI12 images observed by FUV-IMAGE at 1256, 1302 and 1324 UT, December 25, 2000.

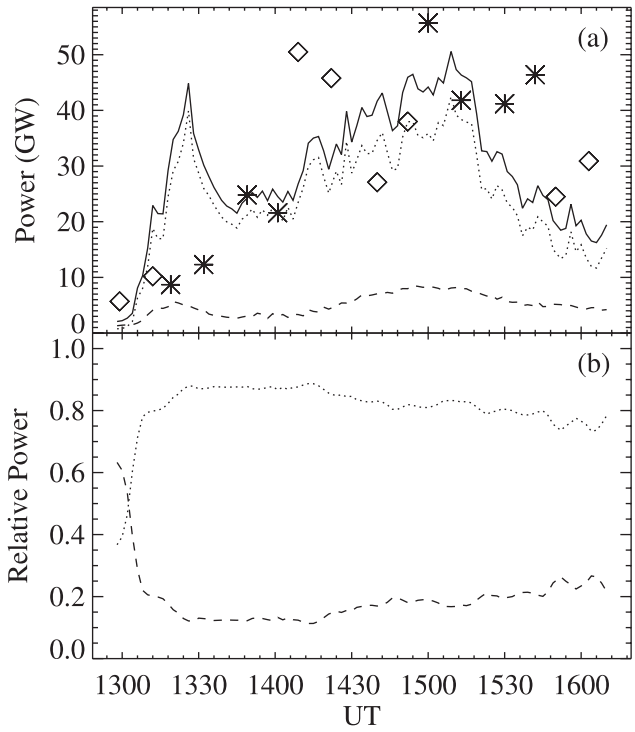

Figure 6. Hemispheric power for December 25, 2000 (panel a). The dotted line is for electrons, the dashed line for protons, and the solid line is the total HP. The IMAGE satellite was observing the North Pole. NOAA-derived HPs are represented by diamonds (North Pole passes) and stars (South Pole passes). Panel b: relative contributions of electrons and protons to HP.

1600 UT. The proton auroral images from SI12 also exhibit an onset at the same location at 1302 UT. As the temporal resolution is ~2 minutes, both onsets must be considered as simultaneous. The hemispheric power (HP) may be slightly underestimated before 1320 UT due to incomplete viewing of the dusk sector of the auroral oval, especially in the SI fields of view. The total HP during the very quiet period before 1300 UT is about 2 GW, less than the lowest value of 5 GW previously observed with POLAR-UVI by *Brittnacher et al.* [1997].

[25] The proton HP reaches a maximum value of 5.6 GW at 1320 UT, while the electron HP reaches a maximum of ~40 GW at 1326 UT. The proton HP thus reaches its maximum significantly before the electron HP. Note that the solar wind characteristics measured 70 minutes earlier (i.e. around 1215 UT) by ACE show a maximum density value (actually reached at 1210 UT) with an IMF Bz component changing sign several times in a few minutes, a positive By and a nearly 0, but decreasing, Bx. After a drop in auroral activity, a second onset took place at 1410 UT in the midnight sector, as observed by the WIC and SI13 imagers. Simultaneously, a proton onset is observed by the SI12 imager at the same location. The solar wind perturbation responsible for that activity surge passed the ACE satellite around ~1300 UT, corresponding to a change of Bz sign from negative to positive values, By varying around 0 and a negative Bx. The plasma density reached a maximum value, however less pronounced than the 1210 UT peak. As seen by the FUV cameras, this second active period reaches its maximal HP around 1510 UT for the electrons, and ~1455 UT for the protons. However, the proton HP was slowly varying, and an accurate estimate of the difference between the proton and electron peak times can hardly be determined. During the time interval between the onset and the first substorm peak, the electron hemispheric input increased faster than the proton one.

[26] Figure 6a also presents the hemispheric power deduced from the TED set of instruments on board the NOAA-TIROS satellites. Data collected by NOAA 12, 14, 15 and 16 were available during this period. The method to calculate the NOAA hemispheric power is sensitive to the orbit configuration, i.e. to the manner the satellite crosses the auroral oval. A correction factor is thus routinely determined to account for a possibly unfavorable configuration. A factor close to 1 characterizes an optimal situation. Other values indicate the magnitude of the correction needed. In the present study, we strictly constrained the NOAA HP values by using only conservative corrective factors ranging between 0.7 and 1.3. The NOAA HP estimates clearly missed the first HP maximum between 1300 UT and 1340 UT, as the NOAA orbit configuration was not optimal at that time. The second part of the event, from 1340 UT to 1600 UT is detected by the NOAA satellites. The NOAA HP values are generally consistent with our FUV values, despite the large scatter affecting the NOAA HPs. However, the peak of the first substorm is missed by NOAA 15 at 1320 UT, because that satellite was sampling the 0200–1300 magnetic local time (MLT) sector, and by NOAA 14 at 1330 UT because that satellite sampled the 0500 through noon to 1500 MLT sector. Thus both satellites missed the location of the core of the substorm onset at 1320. Figure 6b presents the relative contribution of protons and electrons to the total hemispheric power. The proton fraction rapidly decreases from over 20% to ~10% after the first onset. It then slowly increases approximately linearly with time until the end of the substorm. Integrating the proton and electron HPs versus time during the full event from ~1300 UT to ~1610 UT, we deduce that the protons contributed an average 17% to the auroral energy input during this time period.

3.2. November 27, 2000

[27] On November 27, 2000, a substorm onset (visually determined) was observed with the WIC and SI13 instruments at ~0355 UT in the premidnight sector. The proton onset appeared in the premidnight sector as well, at exactly the same location as the electron onset, 2 minutes after the electron onset. The proton activity spread into the post midnight sector while the electron activity developed in the premidnight sector. Figure 7a shows that the hemispheric power rose from ~30 GW to a peak value of ~120 GW. It subsequently dropped down to ~20–30 GW. The FUV HPs are maximum at ~0417 UT for the protons and ~0430 for the electrons. During the time interval around the peak HP value, the protons contributed ~10% to the total HP.

[28] A second onset was measured by the three IMAGE-FUV instruments at ~0725 UT at 00 MLT. Concerning the electrons, the substorm expansion extended both duskward and dawnward, while the proton activity predominantly

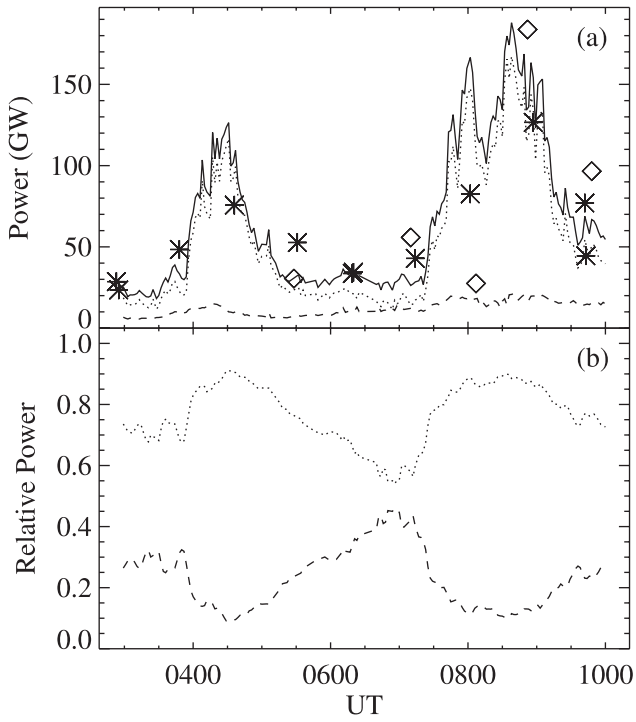

Figure 7. Hemispheric power (panel a) in the northern hemisphere on November 27, 2000. The dotted lines is for electrons, the dashed line for protons, and the solid line is the total HP. NOAA-derived HPs are represented by diamonds (North Pole passes) and stars (South Pole passes). Panel b: relative contributions of electrons and protons to HP.

extended dawnward with a less significant duskward extension. The derived total HP reached a value larger than 150 GW during this substorm. The maximum proton and electron HPs occurred simultaneously at 0840 UT. The Kp index reached a maximum value of 6 during this event and the Dst was less than −64 nT. The provisional AE index was ∼1150 nT at 0800 UT.

[29] The fractional contribution of the protons and electrons are shown in Figure 7b. During the time period from 0300 UT to 1000 UT, the time-integrated proton contribution to the auroral energy input was ∼19%. The hemispheric powers derived from the NOAA measurements present a reasonable agreement with our calculated HPs (Figure 7a). The significant underestimate of HP by NOAA 14 at 0800 UT was because that satellite had sampled the dayside auroral zone between 1500 through noon to 0500 MLT and missed the core of the substorm.

[30] This auroral event was related to solar wind variations detected by the ACE satellite: the solar wind bulk velocity varied between 560 and 640 km s^{-1} between 0200 and 1000 UT (Figure 8). Considering a 600 km s^{-1} bulk velocity, the time needed to travel the distance between the ACE satellite and the Earth is ∼42 minutes. We thus focus on the solar wind characteristics around ∼0315 UT. The solar wind density increased from 10 cm^{-3} at ∼ 0306 UT to 25 cm^{-3} at 0315 UT and 34 cm^{-3} at 0329 UT. Bz decreased from ∼0 nT at 0306 to ∼−15 nT at 0320. In parallel, both Bx and By increased from negative to positive values. The total IMF globally decreased between 0306 and 0329 UT. These solar wind characteristics are consistent with a substorm starting around ∼0355 UT. The second onset is associated with solar wind conditions measured by the ACE satellite around 0645. Later, the solar wind density remained variable between 20 and 30 cm^{-3} until it suddenly jumped to high values of ∼45−55 cm^{-3} and stayed stable between 0755 and 0810 UT. This solar wind pulse presumably reached the Earth at 0830 UT, i.e. a period of very high auroral activity when the HP reached ∼190 GW.

3.3. December 9, 2000

[31] The substorm onset was detected simultaneously by WIC, SI13 and SI12 in the pre-midnight sector at 0527 UT. Kp was moderate (4) and the Dst index was less than −24 nT during the event. AE remained low (less than 250 nT). The calculated hemispheric power for this event is shown in Figure 9a. As seen in Figure 9b, the relative proton contribution varied during the event and reached a minimum value of 10 – 12% near 0550 UT. The mean proton fractional energy input of this event is estimated at ∼19.

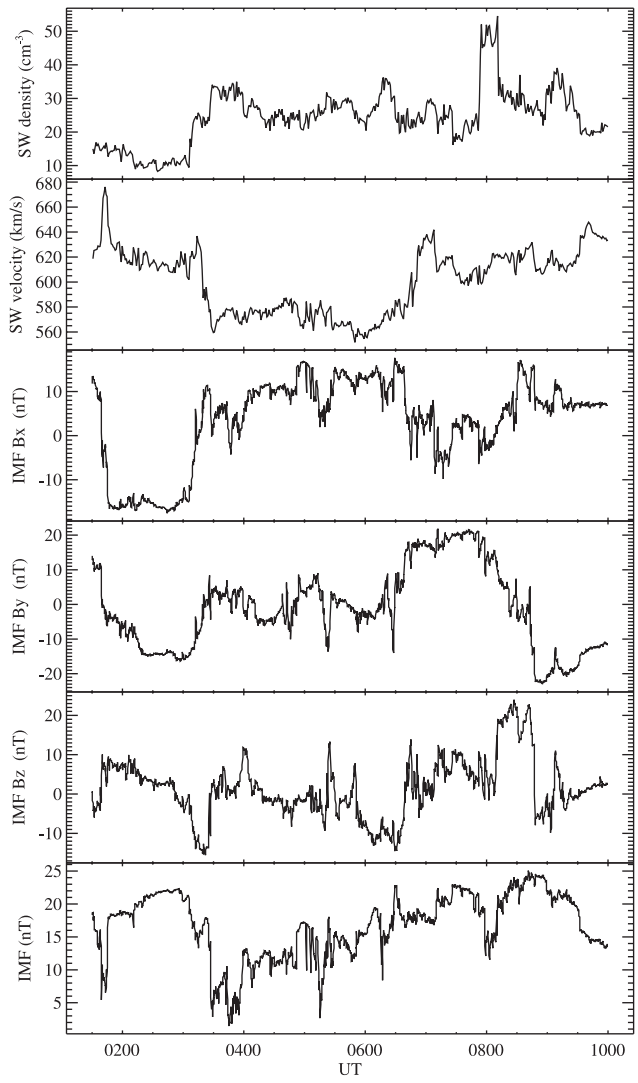

Figure 8. Solar wind characteristics measured by the ACE satellite on November 27, 2000.

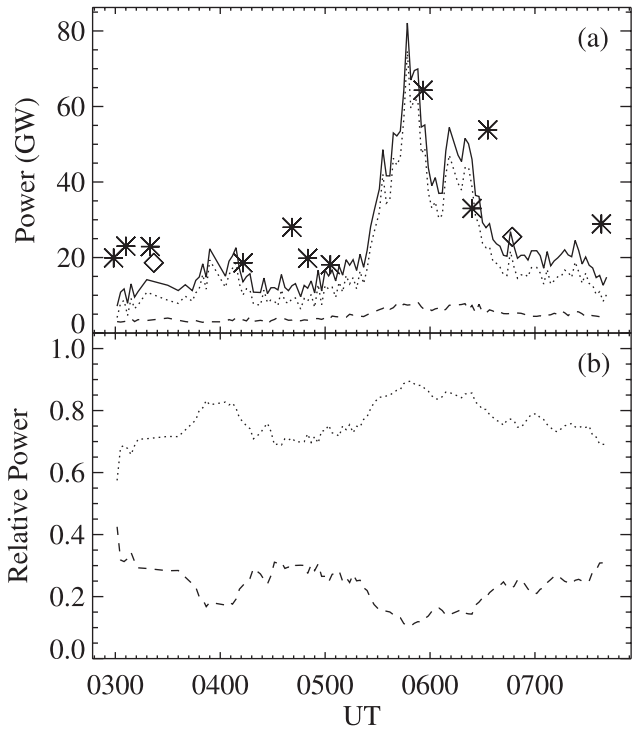

Figure 9. Hemispheric power (panel a) in the northern hemisphere on December 9, 2000. The dotted line is for electrons, the dashed line for protons, and the solid line is the total HP. NOAA-derived HPs are represented by diamonds (North Pole passes) and stars (South Pole passes). Panel b: relative contributions of electrons and protons to HP.

The calculated proton HP did reach its maximal value about 5 minutes later than the electron one. The solar wind velocity measured by the ACE satellite averaged ~645 km s^{-1} during this period, so that the ACE measurements related with this auroral event were made at ~0447 and later. At this time, the solar wind density measured by the ACE satellite was low, between 3 and 5 cm^{-3}. On the basis of a simple temporal analysis, no obvious variation of the solar wind characteristics can unambiguously be identified as responsible for triggering the substorm which occurred some 40 minutes later.

3.4. January 30, 2001

[32] We now analyze a less active period from January 30, 2001. Figure 10a presents the calculated proton and electron hemispheric powers. The Kp index was moderate (3) and Dst was very quiet (less than −6 nT). The NOAA-derived HPs poorly match the IMAGE-FUV values during the quiet periods, and are in fair agreement with FUV values during the active period extending from ~0400 UT to ~0600 UT. Once again, the proton contribution to the IMAGE-derived HP reached its maximum and started decreasing a short time (~4 minutes) before the electron component. Figure 10b presents the relative contribution of proton and electrons for this event. During the entire period, the calculated proton HP contributed ~30% to the total. However, protons contributed only ~15% during the most active period of this substorm.

[33] Both electron and proton onsets took place at 0358 UT in the postmidnight sector. The solar wind bulk velocity was ~450 km s^{-1}, reaching the Earth in ~56 minutes. Around 0300 UT, the ACE satellite measured a stable solar wind density varying between 5 and 6 cm^{-3}. Only Bz changed sign at 0254 UT, rapidly varying from ~−4 nT to ~+1 nT, and rotated several times during the following 15 minutes.

4. Sensitivity of FUV-Derived Hemispheric Power

[34] We now examine the effect of possible sources of uncertainties in the derivation of the HP from IMAGE-FUV. The first one is the perturbation of the atmospheric composition that may not be properly accounted for by the MSIS model. A second one is the characteristic energy of the local proton precipitation.

4.1. Effect of the Atmospheric Composition

[35] The atmospheric composition is modified by the precipitation of energetic particles in the auroral region. Heating due to the energy deposition by the precipitated electrons and protons disturbs the turbopause dynamics, producing upwellings of gas material from a region richer in N_2 and poorer in atomic oxygen. Consequently, the N_2/O ratio may be perturbed by large-scale transport and local auroral energy input as observed by *Hecht et al.* [2000]. Moreover, the detailed photochemical processes controling nitric oxide which partly regulates the thermal structure

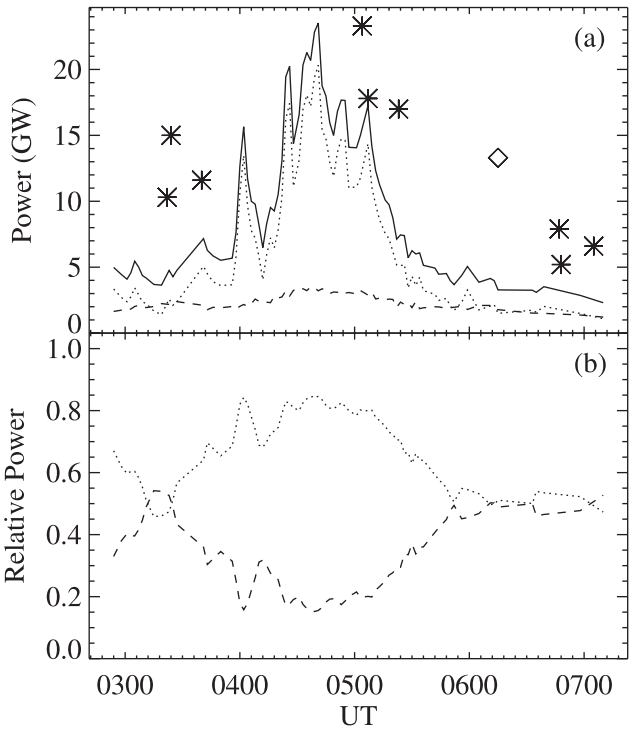

Figure 10. Hemispheric power (panel a) for the northern hemisphere on January 30, 2001. The dotted lines is for electrons, the dashed lines for protons, and the solid line is the total HP. NOAA-derived HPs are represented by diamonds (North Pole passes) and stars (South Pole passes). Panel b: relative contributions of electrons and protons to HP.

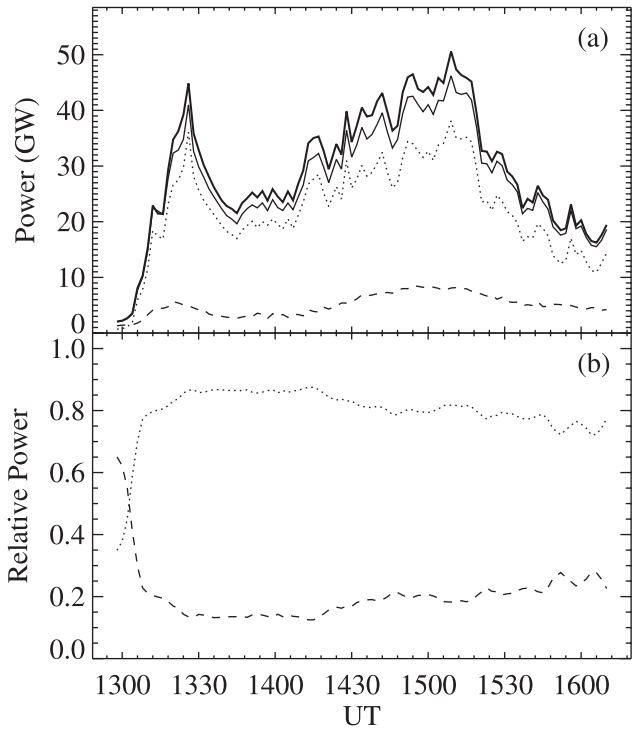

Figure 11. Panel a: hemispheric power on December 25, 2000 calculated assuming an atomic oxygen-depleted atmosphere ([O]/2). Dotted line is for electrons, dashed line for protons, and the light solid line of panel a is the total HP. The total HP of Figure 6a is reproduced here for comparison (thick solid line). Panel b: relative contributions of electrons and protons to HP. This figure can be compared with Figure 6.

[*Kockarts*, 1980] has a very long timescale. Consequently, a complete modeling should account for the history of the auroral activity during several days before the studied events including horizontal transport, and is thus not feasible in this context. We first investigate the effect of an auroral O-depleted atmosphere. Efficiency curves were calculated for the electron excitation of the N_2 LBH and O I 1356-Å emission assuming that the atomic oxygen density profile is 50% of the standard MSIS values. We assume that the temperature profile is not disturbed, so that the N_2 and O_2 density profiles are still given by the MSIS model. The proton efficiency was left unchanged because this change of composition was tested to have a negligible effect (less than 5%) on the auroral Ly α emission. This is because the emitting species are the recombined precipitating protons and not the ambient gas particles and the charge exchange cross section with protons are not largely different for O, O_2 and N_2. Figure 11a shows the calculated HP for the December 25, 2000 case assuming a decrease of the oxygen profile by a factor of 2 similar to the observation of *Hecht et al.* [2000] in active auroras. This curve may be compared to Figure 6a calculated with the standard MSIS model. The proton contribution is unchanged as it is derived from the same photon production efficiency curve in both calculations. The electron HP is less by ~8% at the first peak near 1325 UT and by ~10% at the second peak near 1510 UT. Figure 11b shows that the relative contribution of the protons and electrons is also affected: the calculated contribution of the protons integrated over the full event is 18% in the perturbed case, compared to 17% in Figure 6b. A similar result was obtained when doubling the O_2 and N_2 density profiles, keeping the O density profile given by the MSIS model. Therefore, although no standard reference is available to gauge the different results, it appears that the atmospheric composition disturbance is not a major source of uncertainty in the derivation of the auroral HP from FUV images. However, the composition can have larger local effects.

4.2. Effect of the Assumed Proton Average Energy

[36] The proton energy controls the efficiency value relating the precipitated proton energy flux and the SI12 instrumental count rate. As explained before, an assumption has to be made since three simultaneous FUV measurements (WIC, SI13 and SI12 counts) are available while four quantities (the electron average energy and energy flux and the proton average energy and energy flux) must be determined. The sensitivity of the calculated HP to the assumed proton average energy was tested. We determined the HP associated with six bright consecutive images of December 25, 2000 between 1450 and 1500 UT, i.e. at the time of the peak of the HP, to maximize the signal-to-noise ratio. Figure 12a presents the average HP of the selected six images as a function of the assumed proton average energy. The total HP is insensitive to the proton power above ~25 keV. The calculated proton power is minimum around 3 keV. The relative proton contribution (Figure 12b) is also minimum at ~3 keV, and increases at higher energy. Typical average proton energies given by the *Hardy et al.* [1991] model range between ~0 and 15 keV at Kp = 3,

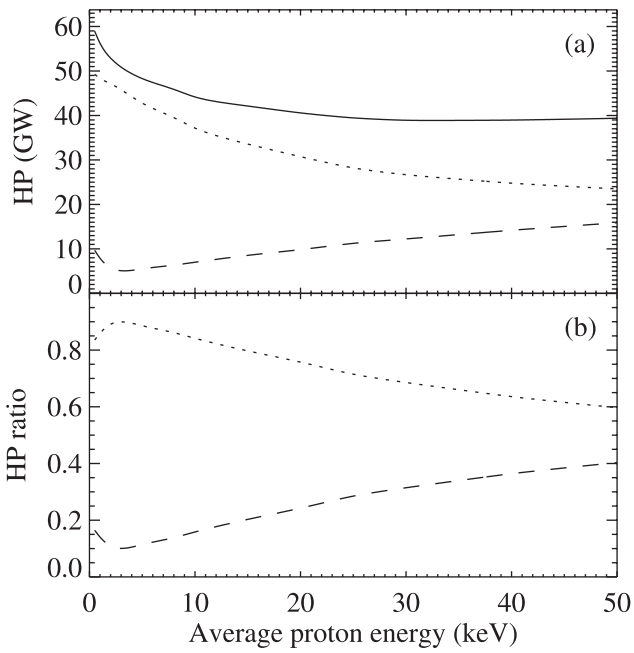

Figure 12. Dependence of the calculated hemispheric power on the assumed mean proton energy calculated for a set of 6 consecutive FUV images on December 25, 2000 event (see text). The solid line represents the total HP. The dotted lines (dashed lines) refer to electrons (protons, respectively) HP (first panel) and fraction (second panel).

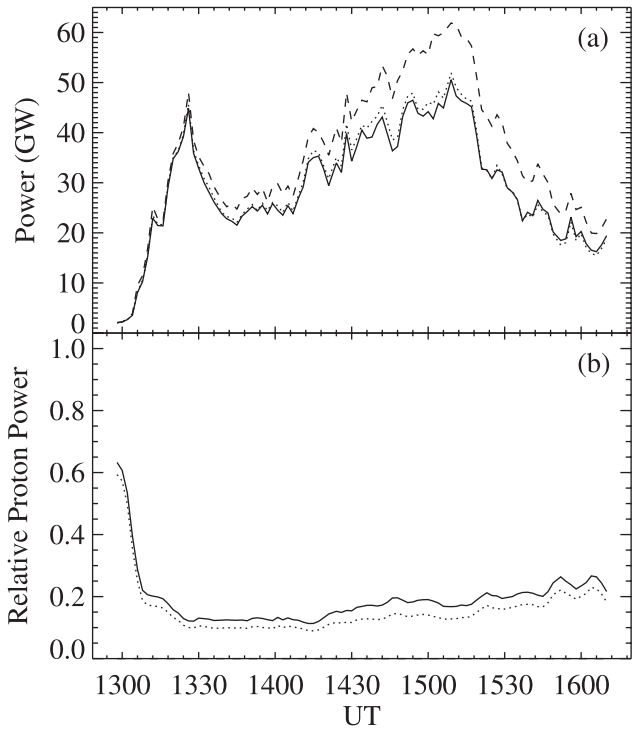

Figure 13. Sensitivity of the calculated hemispheric power for December 25, 2000 to the assumed proton energy. Panel (a) presents the total HP calculated using the standard method (solid line), assuming that all energy flux is carried by electrons (dashed line), and using a fixed (8 keV) proton energy approximation for the entire auroral region (dotted line). Panel (b) shows the relative contribution of protons (same symbols).

depending on latitude and magnetic local time. This sensitivity of the proton HP to the assumed proton energy leaves some uncertainty on the proton relative contribution to the hemispheric power. However, the total HP uncertainty due to this factor is on the order of ±15%.

[37] The effect of neglecting the proton component and consider that only electrons carry the precipitated auroral energy, using only the WIC and SI13 data to calculate the HP was tested for the December 25 case (Figure 13a). It leads to an estimated HP ∼5% to ∼25% larger than the standard procedure which considers protons separately. This overestimate is comparable to the uncertainty associated with the proton average energy hypothesis, although it can be somewhat larger. Figure 13a also shows the time variation of the total HP calculated assuming a constant proton energy of 8 keV for all auroral pixels. The difference with the standard processing is no more than 5%. Figure 13b shows the sensitivity of the relative proton energy flux to the proton energy hypothesis. The assumption of 8 keV protons results in a very small decrease in the calculated proton flux during quiet periods and increases up to about 20% during the active periods.

4.3. Assumption on the Symmetry of the Emitting Layer

[38] The instrumental count rates are converted into energy flux units assuming the emission rate has no horizontal gradient, and is thus spherically symmetric. Another frequently used assumption considers all pixels as if they were observed at the nadir of the instrument. In this case, a measured auroral imager count rate translates into a larger energy flux than if the view angle is accounted for. We examine the uncertainty due to this hypothesis by setting the view angle to 0° (vertical viewing) for all pixels in the December 25, 2000 test case. The difference between the two methods amounts to 12% at the peak of the first substorm and 17% at 1509 UT.

5. Discussion and Conclusions

[39] In this study, we described a method for deriving separately the proton and electron auroral hemispheric power (HP) based on FUV remote sensing of the aurora, using the three IMAGE-FUV instruments (namely WIC, SI-13 and SI-12). The calculated HP compares well with the values based on the NOAA satellite measurements, despite the scatter of those values in some cases. In the four events we considered, the proton and electron onsets were detected simultaneously at the same location and were generally well related to changes in the solar wind characteristics measured by the ACE satellite. The potential effect of neutral composition perturbations due to auroral heating and dynamical effects was tested and found to have limited influence on the total HP and on the proton relative contribution. The assumption on the proton average energy was shown to affect the calculated total HP by ∼15% at most. This uncertainty is comparable to or less than the error made by neglecting the proton precipitation.

[40] FUV-derived time series of the total hemispheric power are generally in good agreement with the NOAA values when the NOAA orbital configuration is favorable. The FUV instrument offer two important advantages. First, the 2-minute time resolution of the FUV is considerably better than the NOAA method which is limited by the orbital period (90 minutes) and the number of available operational spacecraft. This is of special importance during rapid rises of the hemispheric energy input which may not be properly captured by the NOAA data set because, during those times, there is a breakdown in the underlying assumptions in the NOAA approach to computing HP. For example, the time of the substorm onset is only loosely defined from the NOAA data as evidenced in Figures 6, 7, 9 and 10. Second, the set of FUV instruments make it possible to separate the electron and the proton components of the energy injection. Although the characteristic energy of the precipitated protons cannot be determined directly from the FUV observations, reasonable assumptions can be made based on statistical models of auroral proton precipitation.

[41] The relative fraction of the energy input carried by the protons is time dependent and shows significant variation in the course of a substorm. Quiet periods correspond the largest relative proton contribution. As the substorm develops and expands, the proton input increases considerably less than the electron component. Consequently, the fractional proton contribution is minimum during the substorm most active phase. *Mende et al.* [2001] showed the example of a substorm where the total electron precipitation suddenly increased one whole order of magnitude, while the protons increase only about 50%. The intensification of the precip-

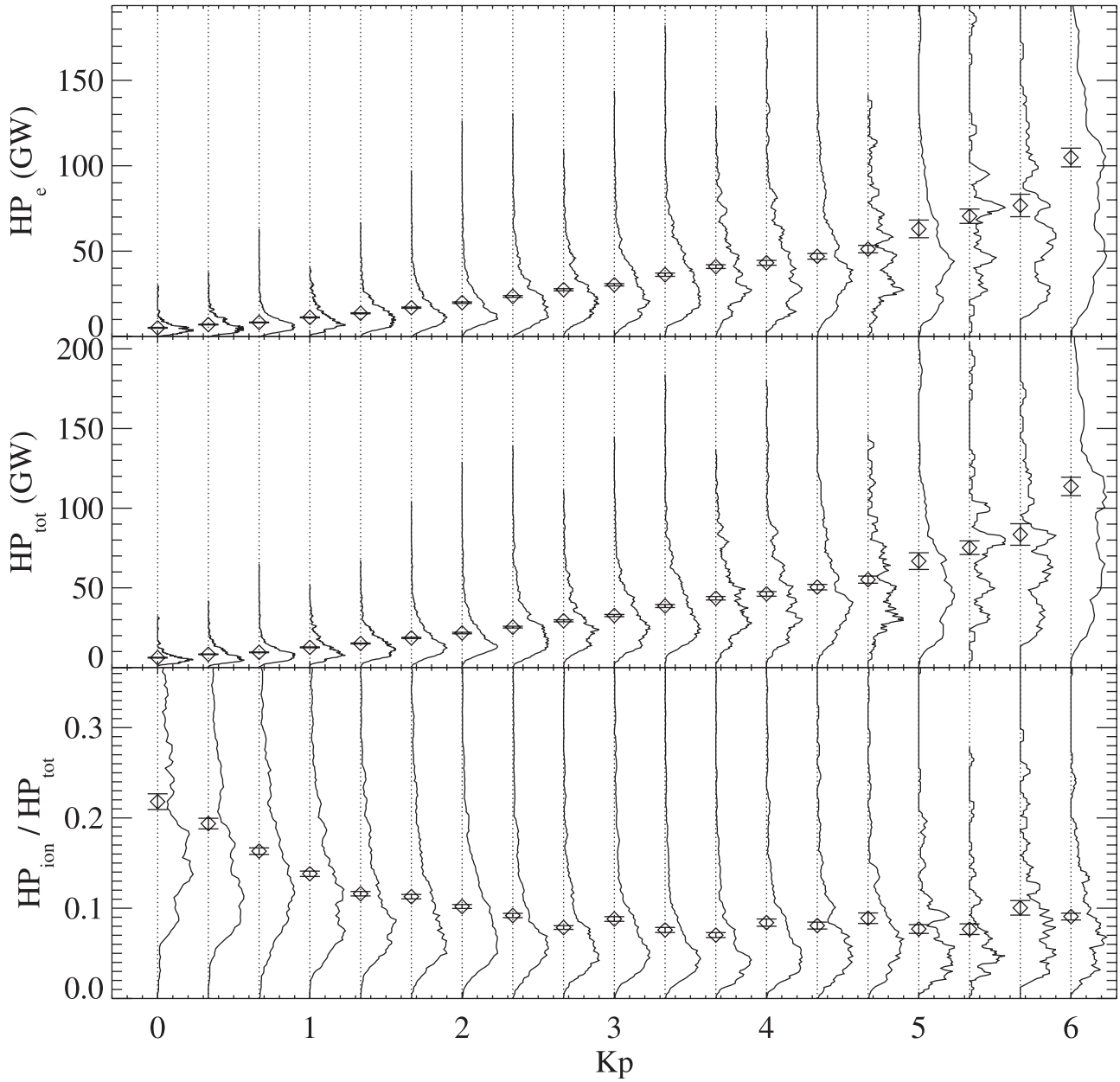

Figure 14. Variation of the auroral hemispheric power in the northern hemisphere as a function of Kp derived from NOAA 15 for year 2000. Top: contribution of electrons only; center: contribution of electrons and protons; bottom: fractional contribution of protons (see text). The thin line shows the statistical distribution function of each quantity for each Kp value, the diamonds are the mean values and the vertical error bars give the 1-σ uncertainty affecting the mean estimation.

itating electrons was relatively short-lived (~10 minutes) while the ENA enhancements, which are mostly indicative of the enhanced trapped particle population, are as long as an hour. Out of 6 substorm events analyzed in this study, 4 showed the proton peak HP occurring 4 to 15 minutes before the electron HP maximum. This point requires a more thorough analysis based on a larger statistical basis.

[42] In order to compare this result with the statistical contribution of protons to the HP, we analyzed the variation with magnetic activity of the NOAA hemispheric power due to electrons only in comparison with the total HP for electrons and protons. Figure 14 shows the dependence versus Kp of the electron HP, the total HP considering both protons and electrons and the fractional contribution of protons to the hemispheric power. Although this fraction shows a wide range of values for a given Kp, the average fraction clearly shows a decreasing trend from 22% at Kp = 0 to 9% at Kp greater than 3. These mean values must be considered as lower limits since only energies less than 20 keV are measured with the TED instrument on board the NOAA-TIROS satellites, with a high energy sensitivity limit of 20 keV. These values must therefore be considered as lower limits. Although never observed globally before, the decrease in the relative proton energy input as the

substorm develops, that is reported here, is thus consistent with these statistical results.

[43] In the study by *Hardy et al.* [1989], the statistical ordering of the DMSP data in terms of 3-hourly Kp indices considerably smoothed the instantaneous value of the electron and proton energy inputs as shown from the comparison of our HP values with the statistically averaged energy inputs from DMSP. This is clearly evident from Figure 13 of *Hardy et al.* [1989] whose values are about two times less than our peak values for an equal Kp index. The smaller fraction of proton input during quiet auroral periods derived from the DMSP model compared to FUV may similarly be a consequence of the averaging process in the *Hardy et al.* [1989] model.

[44] The DMSP database also indicates that the fraction of energy carried by protons strongly depends on MLT with values as large as 44% at 1800 MLT for Kp = 2. Future FUV analysis will concentrate on the distribution of the precipitated power in terms of magnetic latitude and local time and interplanetary magnetic field intensity and orientation.

[46] **Acknowledgments.** J.C.G. is supported by the Belgian National Fund for Scientific Research (FNRS). This work was funded by the PRODEX program of the European Space Agency (ESA) and the Fund for Collective and Fundamental Research (FRFC grants 97-2.4569.97 and 01-2.4569.01). ACE level 2 data were provided by N. F. Ness (MFI) and D. J. McComas (SWEPAM), and the ACE Science Center.
Lou-Chuang Lee and Chin S. Lin thank Stanley Solomon and another reviewer for their assistance in evaluating this paper.

References

Ahn, B. H., S.-I. Akasofu, and Y. Kamide, The joule heat production rate and the particle energy injection rate as a function of the geomagnetic indices *AE* and *AL*, *J. Geophys. Res.*, *88*, 6275, 1983.

Ajello, J. M., and D. E. Shemansky, A reexamination of important N_2 cross sections by electron impact with application to the dayglow: The Lyman-Birge-Hopfield band system and N I (119.99 nm), *J. Geophys. Res.*, *90*, 9845, 1985.

Akasofu, S. I., The development of the auroral substorm, *Planet. Space Sci.*, *12*, 273, 1964.

Brittnacher, M., R. Elsen, and G. Parks, A dayside auroral energy deposition case study using the Polar Ultraviolet Imager, *Geophys. Res. Lett.*, *24*, 991–994, 1997.

Burch, J. L., et al., Views of Earth's magnetosphere with the IMAGE satellite, *Science*, *291*, 619, 2001.

Coumans, V., J.-C. Gérard, B. Hubert, and D. S. Evans, Electron and proton excitation of the FUV aurora: Simultaneous IMAGE and NOAA observations, *J. Geophys. Res.*, *107*, 10.1029/2001JA009233, in press, 2002.

Craven, J. D., and L. A. Frank, The temporal evolution of a small auroral substorm as viewed from high altitudes with Dynamics Explorer 1, *Geophys. Res. Lett.*, *12*, 465–468, 1985.

Frey, H. U., S. B. Mende, C. W. Carlson, J.-C. Gérard, B. Hubert, J. Spann, R. Gladstone, and T. J. Immel, The electron and proton aurora as seen by IMAGE-FUV and FAST, *Geophys. Res. Lett.*, *28*, 1135, 2001.

Fuller-Rowell, T. J., and D. S. Evans, Height-integrated Pedersen and Hall conductivity patterns inferred from the TIROS-NOAA satellite data, *J. Geophys. Res.*, *92*, 7606, 1987.

Gérard, J. C., B. Hubert, D. V. Bisikalo, and V. I. Shematovich, A model of the Lyman-α line profile in the proton aurora, *J. Geophys. Res.*, *105*, 15,795, 2000.

Gérard, J. C., B. Hubert, D. V. Bisikalo, V. I. Shematovich, H. U. Frey, S. B. Mende, M. Meurant, G. R. Gladstone, and C. W. Carlson, Observation of the proton aurora with IMAGE FUV imager and simultaneous ion flux in situ measurements, *J. Geophys. Res.*, *106*, 28,939–28,948, 2001.

Gladstone, G. R., et al., Stellar calibration of the WIC and SI Imagers and the GEO photometers on IMAGE/FUV, *Eos Trans. AGU*, *81*(48), Fall Meet. Suppl., SM72A-06, 2000.

Hardy, D. A., M. S. Gussenhoven, and D. Brautigam, A statistical model of auroral ion precipitation, *J. Geophys. Res.*, *94*, 370, 1989.

Hardy, D. A., W. McNeil, M. S. Gussenhoven, and D. Brautigam, A statistical model of auroral ion precipitation, 2, Functional representation of the average patterns, *J. Geophys. Res.*, *96*, 5539, 1991.

Hecht, J. H., D. L. McKenzie, A. B. Christensen, D. J. Strickland, J. P. Thayer, and J. Watermann, Simultaneous observations of lower thermospheric composition change during moderate auroral activity from Kangerlussuaq and Narsarsuaq, Greenland, *J. Geophys. Res.*, *105*, 27,109, 2000.

Hedin, A. E., Extension of the MSIS thermosphere model into the middle and lower atmosphere, *J. Geophys. Res.*, *96*, 1159, 1991.

Hubert, B., J.-C. Gérard, D. V. Bisikalo, V. I. Shematovich, and S. C. Solomon, The role of proton precipitation in the excitation of auroral FUV emissions, *J. Geophys. Res.*, *106*, 21,475, 2001.

Kockarts, G., Nitric oxyde cooling in the terrestrial thermosphere, *Geophys. Res. Lett.*, *7*, 137, 1980.

Lu, G., et al., Global energy deposition during the January 1997 magnetic cloud event, *J. Geophys. Res.*, *103*, 11,685, 1998.

Lummerzheim, D., M. Brittnacher, and D. Evans, High time resolution study of the hemispheric power carried by energetic electrons into the ionosphere during the May 19/20, 1996 auroral activity, *Geophys. Res. Lett.*, *24*, 987, 1997.

Mende, S. B., et al., Far ultraviolet imaging from the IMAGE spacecraft, 1, System design, *Space Sci. Rev.*, *91*, 243, 2000a.

Mende, S. B., et al., Far ultraviolet imaging from the IMAGE spacecraft, 3, Spectral imaging of Lyman alpha and OI 135.6 nm, *Space Sci. Rev.*, *91*, 287, 2000b.

Mende, S. B., H. U. Frey, M. Lampton, J. C. Gérard, B. Hubert, S. Fuselier, J. Spann, G. R. Gladstone, and J. L. Burch, Global observations of proton and electron auroras in a substorm, *Geophys. Res. Lett.*, *28*, 1139, 2001.

Østgaard, N., R. R. Vondrak, J. W. Gjeroev, and G. Germany, A relation between the energy deposition by electron precipitation and geomagnetic indices during substorms, *J. Geophys. Res.*, *107*, 10.1029/2001JA002003, in press, 2002.

Rees, M. H., *Physics and Chemistry of the Upper Atmosphere*, Cambridge Univ. Press, New York, 1989.

Richmond, A. D., Y. Kamide, and S.-I. Akasofu, Global measures of ionospheric electrodynamic activity inferred from combined incoherent scatter radar and ground magnetometer observations, *J. Geophys. Res.*, *95*, 1061, 1990.

Roble, R. G., E. C. Ridley, A. D. Richmond, and R. E. Dickinson, A coupled thermosphere/ionosphere general circulation model, *Geophys. Res. Lett.*, *15*, 1325, 1988.

Singh, V., and J. C. Gérard, The thermospheric heating efficiency under electron bombardment conditions, *Planet. Space Sci.*, *30*, 1083–1089, 1982.

Solomon, S. C., Auroral particle transport using Monte Carlo and hybrid methods, *J. Geophys. Res.*, *106*, 107, 2001.

Solomon, S. C., P. B. Hays, and V. Abreu, The auroral 6300 Å emission: Observation and modeling, *J. Geophys. Res.*, *93*, 9867, 1988.

Vallance-Jones, A., *Aurora*, D. Reidel, Norwell, Mass., 1974.

D. S. Evans, NOAA Space Environment Center, Boulder, CO, USA. (devans@sec.noaa.gov)

H. U. Frey, T. J. Immel, and S. B. Mende, Space Sciences Laboratory, University of California, Grizzly Peak Boulevard at Centennial Drive, Berkeley, CA 94720, USA. (hfrey@ssl.berkeley.edu; immel@ssl.berkeley.edu; mende@ssl.berkeley.edu)

J.-C. Gérard, B. Hubert, and M. Meurant, Laboratoire de Physique Atmosphérique et Planétaire, Université de Liège, 5 Avenue de Cointe, B-4000 Liège-Ougrée, Belgium. (jc.gerard@ulg.ac.be; B.hubert@ulg.ac.be; mmeurant@ulg.ac.be)